IRS-Aided SWIPT: Joint Waveform, Active and Passive Beamforming Design

Yang Zhao, *Member, IEEE* and Bruno Clerckx, *Senior Member, IEEE*

***Abstract*—The performance of Simultaneous Wireless Information and Power Transfer (SWIPT) is mainly restricted by the strength of the received Radio-Frequency (RF) signal. To tackle this problem, we introduce a low-power Intelligent Reflecting Surface (IRS) that compensates the propagation loss and boosts the energy efficiency with a passive beamforming gain. This paper investigates an IRS-aided Orthogonal Frequency Division Multiplexing (OFDM) SWIPT system based on a practical nonlinear energy harvester model, where a multi-antenna Access Point (AP) transmits information and energy simultaneously to a single-antenna user under the assist of IRS. We aim to maximize the Rate-Energy (R-E) region via jointly optimizing the transmit waveform at the AP, the reflection coefficients at the IRS, and the power splitting ratio at the user. The performance of the proposed waveform and beamforming design is compared with those of no IRS, fixed IRS and ideal frequency-selective (FS) IRS, and we confirm that due to rectifier nonlinearity, a dedicated power signal can be beneficial to energy harvesting (EH) while the optimal transceiving strategy depends on the system configuration. Simulation results also demonstrate that the proposed adaptive IRS design brings significant R-E enhancement over benchmark schemes for broadband transmission, and the optimal IRS can be approximated in closed form with negligible performance loss for narrowband transmission.**

***Index Terms*—Wireless information and power transfer, intelligent reflecting surface, waveform design, active and passive beamforming.**

I. Introduction

A. Simultaneous Wireless Information and Power Transfer

With the great advance in communication performance, the main challenge of wireless network has come to energy supply. Most existing mobile devices are powered by batteries that require frequent charging or replacement, which leads to high maintenance cost thus restricts the scale of networks. Although solar energy and inductive coupling has become popular alternatives, the former depends on the environment while the latter has a very short operation range. Simultaneous Wireless Information and Power Transfer (SWIPT) is a promising solution to connect and power mobile devices via electromagnetic (EM) waves in the Radio-Frequency (RF) band. It provides low power in μW level but broad coverage up to hundreds of meters in a sustainable and controllable manner [1]. The decreasing trend of electronic power consumption also boosts the paradigm shift from dedicated power source to Wireless Power Transfer (WPT) and SWIPT.

The concept of SWIPT were first cast in [2], where the authors investigated the Rate-Energy (R-E) tradeoff for a flat Gaussian channel and typical discrete channels. Two practical receiver structures were then proposed in [3], namely Time Switching (TS) that switches between Energy Harvesting (EH) and Information Decoding (ID) modes, and Power Splitting (PS) that splits the received signal into individual components. On top of this, [4] characterized the R-E region for a Multiple-Input Multiple-Output (MIMO) broadcast system under TS and PS setup. Information and power beamforming was then considered in multiuser Multi-Input Single-Output (MISO) systems to maximize the Weighted Sum-Power (WSP) subjective to Signal-to-Interference-plus-Noise Ratio (SINR) constraints [5]. Motivated by this, [6] investigated fundamental transceiver modules, scheduling schemes, and interference management for SWIPT systems. However, [7] pointed out that the Radio Frequency-to-Direct Current (RF-to-DC) conversion efficiency depends on the harvester input power level. The authors also suggested a curve-fitting based parametric harvester model and proposed an iterative resource allocation algorithm. From another perspective, [8], [9] demonstrated that multisine waveform is more suitable for WPT as it outperforms single tone in both operation range and RF-to-DC efficiency. [10] derived a tractable nonlinear harvester model based on the Taylor expansion of diode I-V characteristics, then implemented waveform design for WPT. Simulation and experiments demonstrated the benefit of modelling rectifier nonlinearity in system design [11], [12]. The work was extended to SWIPT in [13] where a superposition of modulated information waveform and multisine power waveform was employed to enlarge the R-E region. In contrast, [14] suggested an adaptive dual-mode SWIPT, which alternates between single-tone transmission that exploits conventional modulation for high-rate applications and multisine transmission that encodes the information in the Peak-to-Average Ratio (PAPR) for power-demanding applications. Modulation and coding schemes for SWIPT also receive much attention. By assuming On-Off-Keying (OOK) where bit 1 carries energy, [15] compared unary and Run-Length-Limited (RLL) code in terms of rate versus battery overflow/underflow probability. It suggested that WPT should be activated only at constellation points with a large offset. Also, a learning approach [16] demonstrated that the offset of the power symbol is positively correlated to the harvester energy constraint, while the optimal information symbols are symmetrically distributed around the origin. It confirmed that the superposed waveform is effective to enlarge R-E region when considering rectifier nonlinearity. As for the network design, [17] proposed a cooperative SWIPT Non-Orthogonal Multiple Access (NOMA) protocol with three user selection schemes such that the strong user assists the EH of the weak user. SWIPT based on Rate

The authors are with the Department of Electrical and Electronic Engineering, Imperial College London, London SW7 2AZ, U.K. (e-mail: yang.zhao18@imperial.ac.uk; b.clerckx@imperial.ac.uk).

Splitting (RS) technique was also explored in [18].

B. Intelligent Reflecting Surface

Intelligent Reflecting Surface (IRS) adapts the wireless channel to increase spectrum and energy efficiency. In practice, an IRS consists of multiple individual reflecting elements that adjust the amplitude and phase of the incident signal through passive beamforming. Different from relay and backscatter, IRS assists the primary transmission using fully passive components, thus consumes less power with no additional thermal noise but is limited to frequency-flat (FF) reflection. Although Frequency-Selective Surface (FSS) has received much attention for wideband communications, it is different from IRS as active FSS requires RF-chains [5], [19] while passive FSS has fixed physical characteristics thus not adjustable [20].

Inspired by the advance of real-time reconfigurable metamaterials in [21], [22] introduced a programmable metasurface that steers or polarizes the EM wave at specific frequency to mitigate signal attenuation. At the same time, [23] constructed an adjustable reflect array that ensures reliable millimeter-wave (mmWave) communication based on a beam-searching algorithm to reduce indoor signal blockage. Motivated by this, [24], [25] introduced an IRS-assisted MISO system and proposed a beamforming algorithm that jointly optimizes the precoder at the Access Point (AP) and the phase shifts at the IRS to maximize Signal-to-Noise Ratio (SNR). The active and passive beamforming problem was extended to the discrete phase shift case [26] and the multiuser case [27]. The application of IRS in interference cancellation and secure communication are also investigated in [28], [29]. In [30], channel estimation for Time-Division Duplex (TDD) systems was carried through a two-stage Minimum Mean Squared Error (MMSE)-based protocol that sequentially estimates the cascaded channel of each IRS element with the others switched off. Starting from the impedance equation, [31] investigated the influence of phase shift on the reflection amplitude and proposed a parametric IRS model via curve fitting. Recent research also explored the opportunity of integrating IRS with Orthogonal Frequency-Division Multiplexing (OFDM) systems. [32] exploited spatial correlation to reduce estimation overhead and design complexity by assuming adjacent elements share a common reflection coefficient. On top of this, group-based OFDM channel estimation was investigated in [33]. By adjusting IRS over time slots, [34] introduced artificial diversity within coherence time and investigated resource allocation and IRS configuration per Resource Block (RB). Real-time high-definition video transmission was performed over a prototype constructed with Positive Intrinsic-Negative (PIN) diodes, which demonstrated the feasibility and benefit of IRS at GHz and mmWave frequency [35].

C. IRS-aided SWIPT

The effective channel enhancement and low power consumption of IRS are expected to bring more opportunities to SWIPT. Supposing energy interference and linear harvester model, [36] proved that at most one energy beam is required to maximize the WSP subject to SINR constraints. The fairness issue was then considered in [37], which maximize the minimum output power with the assumption of perfect energy interference cancellation. [38] proposed a novel penalty-based algorithm, whose inner layer employs Block Coordinate Descent (BCD) method to update transmit precoders and IRS phase shifts while the outer layer updates the penalty coefficients. It demonstrated that Line-of-Sight (LoS) links can boost the harvested power, as the rank-deficient channels are highly correlated such that a single energy stream can satisfy the energy constraints of all ERs. In [39], the authors proposed low-complexity BCD algorithms to maximize the Weighted Sum-Rate (WSR) of Information Receivers (IRs) subject to the power constraint at Energy Receivers (ERs). However, most existing IRS-assisted SWIPT papers focused on narrow-band transmission for separated IRs and ERs based on an oversimplified linear harvester model.

D. Objective and Methodology

In this paper, we study an IRS-aided downlink MISO SWIPT system where the IRS assists the information and energy transmission of a single user. A multicarrier unmodulated power waveform (deterministic multisine) is superposed to a multicarrier modulated information waveform (e.g. OFDM) to boost the energy transfer efficiency without creating additional interference. The transmit waveform, IRS phase shift and receive splitting ratio are jointly optimized to maximize the R-E tradeoff. Different from previous research, this paper focus on multicarrier IRS-SWIPT and investigates the fundamental impact of harvester nonlinearity on passive beamforming design. The R-E region characterization problem is transformed into multiple current maximization problems subject to different rate constraints. To reduce the design complexity, we propose an Alternating Optimization (AO) algorithm that updates the channel and transceiver iteratively based on Semidefinite Relaxation (SDR) and Geometric Programming (GP) techniques. Numerical results showed that SDR is tight and the proposed algorithm can find a stationary point for all tested channel realizations. We demonstrate that dedicated power waveform can boost the energy transmission efficiency such that TS and PS are preferred at low SNR and high SNR, respectively. Also, IRS brings a significant channel amplification and R-E enhancement especially when deployed next to the transmitter or the receiver. Finally, the proposed adaptive IRS design outperformed the benchmark schemes for broadband transmission, and the optimal IRS can be approximated in closed form for narrowband SISO transmission.

Organization: The rest of this paper is organized as follows. Section II introduces the signal, channel, decoder, harvester, and R-E tradeoff models of the IRS-aided SWIPT system. Section III tackles the waveform, active and passive beamforming optimization. Section IV presents simulation results to evaluate the proposed design. Section [TODO] concludes the paper.

Notations: Scalars are denoted by italic letters, vectors are denoted by bold lower-case letters, and matrices are denoted by bold upper-case letters. $\mathbb{C}^{x\times y}$ denotes the subspace spanned by complex $x \times y$ matrices. $\Re\{\cdot\}$ and $\Im\{\cdot\}$ stand for the real and imaginary part of a complex number or variable, respectively.

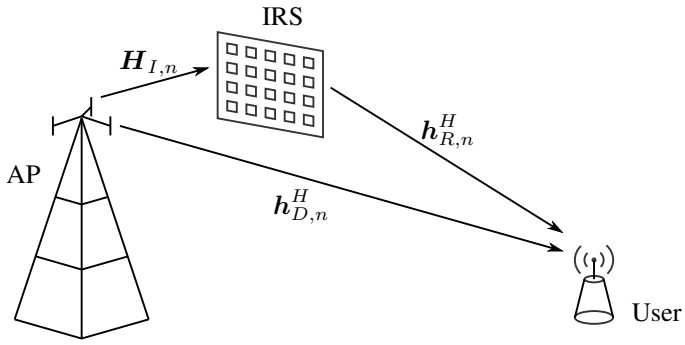

Fig. 1. An IRS-aided OFDM SWIPT system

$(\cdot)^*$, $(\cdot)^T$ and $(\cdot)^H$ represent the conjugate, transpose, and conjugate transpose operators, respectively. $\mathcal{A}\{\cdot\}$ extracts the DC component of a signal, and $\mathcal{E}_X\{\cdot\}$ takes the expectation over the distribution of the random variable X (X may be omitted for simplicity). For a scalar x, $|x|$ denotes its absolute value. For a vector $\boldsymbol{x}$, $\|\boldsymbol{x}\|$ refers to its Euclidean norm, $\arg(\boldsymbol{x})$ refers to its argument vector, and $\mathrm{diag}(\boldsymbol{x})$ refers to a square diagonal matrix with the elements of $\boldsymbol{x}$ on the main diagonal. For a general matrix $\boldsymbol{M}$, $\mathrm{rank}(\boldsymbol{M})$ denotes it rank. For a square matrix S, $\mathrm{Tr}(\boldsymbol{S})$ denotes its trace, and $\boldsymbol{S} \succeq 0$ means that $\boldsymbol{S}$ is positive semi-definite. The distribution of a Circularly Symmetric Complex Gaussian (CSCG) random vector with mean $\boldsymbol{\mu}$ and covariance matrix $\boldsymbol{\Sigma}$ is denoted by $\mathcal{CN}(\boldsymbol{\mu}, \boldsymbol{\Sigma})$ where $\sim$ stands for "distributed as". We also denote $(\cdot)^\star$ and $(\cdot)^{(i)}$ as stationary solution and variable value at iteration i, respectively.

II. System Model

As shown in Fig. 1, we consider an IRS-aided SWIPT system where a M-antenna AP delivers information and power simultaneously, through a L-reflector IRS, to a single-antenna user over N orthogonal evenly-spaced subbands with center frequency f_n ($n = 1, \ldots, N$). Perfect Channel State Information (CSI) with negligible training overhead is assumed to explore the upper bound of the proposed design. A quasi-static block fading channel model is considered for all links, and we focus on one particular block where the channels are approximately unchanged. Two practical co-located receiver architectures are compared in terms of R-E region. Specifically, TS divides each time slot into orthogonal data and energy slots and performs a time sharing between WPT and Wireless Information Transfer (WIT). In comparison, PS splits the received signal into individual ID and EH streams such that the splitting ratio ρ is coupled with waveform and IRS design. Perfect synchronization is assumed among the three parties in both scenarios, and signals reflected by IRS for two and more times are omitted. We also assume the noise is too small to harvest.

A. Transmit Signal

Denote $\tilde{x}_{I,n}(t)$ as the information symbol transmitted over subband n, which follows a capacity-achieving i.i.d. CSCG distribution with zero mean and unit variance, namely $\tilde{x}_{I,n} \sim \mathcal{CN}(0,1)$. The superposed transmit signal on antenna m ($m = 1, \ldots, M$) at time t is

$$x_m(t) = \Re\left\{\sum_{n=1}^{N} \left(w_{I,n,m}\tilde{x}_{I,n}(t) + w_{P,n,m}\right) e^{j2\pi f_n t}\right\} \quad (1)$$

where $w_{I/P,n,m}$ denotes the weight on the information and power signal transmitted by antenna m at subband n. Define $\boldsymbol{w}_{I/P,n} = [w_{I/P,n,1}, \ldots, w_{I/P,n,M}]^T \in \mathbb{C}^{M\times 1}$ by stacking up weights across all antennas. Therefore, the transmit information and power signals write as

$$\boldsymbol{x}_I(t) = \Re\left\{\sum_{n=1}^{N} \boldsymbol{w}_{I,n}\tilde{x}_{I,n}(t)e^{j2\pi f_n t}\right\} \quad (2)$$

$$\boldsymbol{x}_P(t) = \Re\left\{\sum_{n=1}^{N} \boldsymbol{w}_{P,n}e^{j2\pi f_n t}\right\} \quad (3)$$

B. Composite Channel

At subband n, denote the AP-user direct channel as $\boldsymbol{h}_{D,n}^H \in \mathbb{C}^{1\times M}$, AP-IRS incident channel as $\boldsymbol{H}_{I,n} \in \mathbb{C}^{L\times M}$, and IRS-user reflective channel as $\boldsymbol{h}_{R,n}^H \in \mathbb{C}^{1\times L}$. At the IRS, element l ($l = 1, \ldots, L$) redistributes the incoming signal by adjusting the reflection amplitude $\gamma_l \in [0,1]$ and phase shift $\theta_l \in [0, 2\pi)$ [1]. On top of this, the IRS matrix collects the reflection coefficients onto the main diagonal entries as $\boldsymbol{\Theta} = \mathrm{diag}(\gamma_1 e^{j\theta_1}, \ldots, \gamma_L e^{j\theta_L}) \in \mathbb{C}^{L\times L}$. The extra link introduced by IRS can be modeled as a concatenation of the AP-IRS incident channel, IRS reflection, and IRS-user reflective channel. On top of this, the total composite channel is obtained by superposing the IRS-aided extra channel to the AP-user direct channel as

$$\boldsymbol{h}_n^H = \boldsymbol{h}_{D,n}^H + \boldsymbol{h}_{R,n}^H\boldsymbol{\Theta}\boldsymbol{H}_{I,n} = \boldsymbol{h}_{D,n}^H + \boldsymbol{\phi}^H\boldsymbol{V}_n \quad (4)$$

where $\boldsymbol{\phi} = [\gamma_1 e^{j\theta_1}, \ldots, \gamma_L e^{j\theta_L}]^H \in \mathbb{C}^{L\times 1}$ and $\boldsymbol{V}_n = \mathrm{diag}(\boldsymbol{h}_{R,n}^H)\boldsymbol{H}_{I,n} \in \mathbb{C}^{L\times M}$. Note the conjugate transpose in the notation of $\boldsymbol{\phi}$ makes its entries the complex conjugate of the diagonal entries of $\boldsymbol{\Theta}$.

C. Receive Signal

At the single-antenna receiver, the total received signal $y(t) = y_I(t) + y_P(t)$ captures the contribution of information and power components over N subbands, where

$$y_I(t) = \Re\left\{\sum_{n=1}^{N} \boldsymbol{h}_n^H\boldsymbol{w}_{I,n}\tilde{x}_{I,n}(t)e^{j2\pi f_n t}\right\} \quad (5)$$

$$y_P(t) = \Re\left\{\sum_{n=1}^{N} \boldsymbol{h}_n^H\boldsymbol{w}_{P,n}e^{j2\pi f_n t}\right\} \quad (6)$$

[1]To investigate the performance upper bound of IRS, we suppose the reflection coefficient is maximized $\gamma_l = 1\ \forall l$ while the phase shift is a continuous variable over $[0, 2\pi)$.

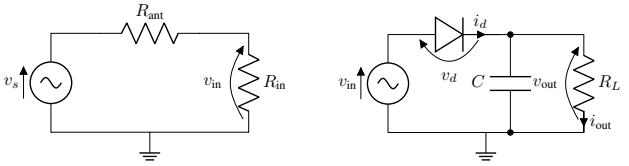

(a) Antenna equivalent circuit (b) A single diode rectifier

Fig. 2. Rectenna circuits

D. Information Decoder

A major benefit of the superposed waveform is that the determined power waveform creates no interference to the information waveform. Therefore, the achievable rate writes as

$$R(\boldsymbol{\phi}, \boldsymbol{w}_I, \rho) = \sum_{n=1}^{N} \log_2 \left(1 + \frac{(1-\rho)|\boldsymbol{h}_n^H \boldsymbol{w}_{I,n}|^2}{\sigma_n^2}\right) \quad (7)$$

where ρ is the power splitting ratio for the energy harvester, σ_n^2 is the variance of the total noise (RF-band and RF-to-baseband conversion) on tone n. Rate 7 is achievable with either waveform cancellation or translated demodulation [40].

E. Energy Harvester

In this section, we briefly revisit a tractable nonlinear rectenna model that relates the harvester output DC current to the received waveform [10], [40]. Fig. 2a illustrates the equivalent circuit of a lossless antenna, where the incoming signal creates an voltage source $v_s(t)$ and the antenna has an impedance R_{ant}. Let R_{in} be the total input impedance of the rectifier and matching network, and we assume the voltage across matching network is negligible. When perfectly matched ($R_{\text{in}} = R_{\text{ant}}$), the rectifier input voltage is $v_{\text{in}}(t) = y(t)\sqrt{\rho R_{\text{ant}}}$.

Rectifiers consist of nonlinear components as diode and capacitor to produce DC output and store energy [41], [42]. Consider a simplified rectifier in Fig. 2b where a single series diode is followed by a low-pass filter with a parallel load. Denote i_s as the reverse bias saturation current, n' as the diode ideality factor, v_t as the thermal voltage, $v_d(t) = v_{\text{in}}(t) - v_{\text{out}}(t)$ as the voltage across the diode where $v_{\text{out}}(t)$ is the output voltage across the load. A Taylor expansion of the diode characteristic equation $i_d(t) = i_s(e^{v_d(t)/n'v_t} - 1)$ around a quiescent operating point a writes as $i_d(t) = \sum_{i=0}^{\infty} k_i'(v_d(t) - a)^i$, where $k_0' = i_s(e^{a/n'v_t} - 1)$ and $k_i' = i_s e^{a/n'v_t}/i!(n'v_t)^i$ for $i = 1, \ldots, \infty$. Note that this small-signal expansion model is only valid for the non-linear operation region, and the I-V relationship would be linear if the diode behavior is dominated by the load [10]. Also, an ideal low-pass filter with steady-state response can provide a constant v_{out} that depends on the peak of $v_{\text{in}}(t)$ [43]. Therefore, a proper choice of the operating voltage drop is $a = \mathcal{E}\{v_d(t)\} = -v_{\text{out}}$ such that

$$i_d(t) = \sum_{i=0}^{\infty} k_i' \rho^{i/2} R_{\text{ant}}^{i/2} y(t)^i \quad (8)$$

By discarding the non-DC components, taking expectation over symbol distribution, and truncating 8 to the n_0-th order, we approximate the average output DC current for a given channel as

$$i_{\text{out}}(t) = \mathcal{A}\{i_d(t)\} \approx \sum_{i=0}^{n_0} k_i' \rho^{i/2} R_{\text{ant}}^{i/2} \mathcal{E}\left\{\mathcal{A}\left\{y(t)^i\right\}\right\} \quad (9)$$

With the assumption of evenly-spaced frequencies, it holds that $\mathcal{A}\left\{y(t)^i\right\} = 0$ for odd i thus the related terms has no contribution to DC output. However, k_i' is still a function of i_{out}, and [10] proved that maximizing a truncated i_{out} is equivalent to maximizing a monotonic function

$$z(\boldsymbol{\phi}, \boldsymbol{w}_I, \boldsymbol{w}_P, \rho) = \sum_{i \text{ even}, i \geq 2}^{n_0} k_i \rho^{i/2} R_{\text{ant}}^{i/2} \mathcal{E}\left\{\mathcal{A}\left\{y(t)^i\right\}\right\} \quad (10)$$

where $k_i = i_s/i!(nv_t)^i$. It can be observed that the traditional linear harvester model, where the output DC power equals the sum of the power harvested on each frequency, is a special case of 10 with $n_0 = 2$. However, due to the coupling among different frequencies, some high-order terms also cancel out non-DC components thus contribute to the output DC power. In other words, even terms with $i \geq 4$ account for the nonlinear behavior of the diode. For simplicity, we let $\beta_2 = k_2 R_{\text{ant}}$, $\beta_4 = k_4 R_{\text{ant}}^2$ and choose $n_0 = 4$ to investigate fundamental nonlinearity. Note that $\mathcal{E}\left\{|\tilde{x}_{I,n}|^2\right\} = 1$ but $\mathcal{E}\left\{|\tilde{x}_{I,n}|^4\right\} = 2$, which can be interpreted as a modulation gain on the nonlinear terms of the output DC current.

Inspired by [44], we stack up channel and waveform vectors over all subbands as $\boldsymbol{h} = [\boldsymbol{h}_1^H, \ldots, \boldsymbol{h}_N^H]^H \in \mathbb{C}^{MN \times 1}$, $\boldsymbol{w}_{I/P} = [\boldsymbol{w}_{I/P,1}^H, \ldots, \boldsymbol{w}_{I/P,N}^H]^H \in \mathbb{C}^{MN \times 1}$. Moreover, let $\boldsymbol{W}_{I/P,n}$ keep the n-th ($n = -N+1, \ldots, N-1$) block diagonal of $\boldsymbol{W}_{I/P} = \boldsymbol{w}_{I/P}\boldsymbol{w}_{I/P}^H$ and null the remaining entries, where the blocks are of size $M \times M$. On top of this, z is reduced to 11 and the corresponding DC terms are expressed in 12 – 15.

F. Rate-Energy Region

Define the achievable R-E region as

$$C_{R_{\text{ID}}-I_{\text{EH}}}(P) \triangleq \Big\{(R_{\text{ID}}, I_{\text{EH}}) : R_{\text{ID}} \leq R, I_{\text{EH}} \leq z, \frac{1}{2}\left(\|\boldsymbol{w}_I\|^2 + \|\boldsymbol{w}_P\|^2\right) \leq P\Big\} \quad (16)$$

where P is the average transmit power budget and the coefficient $1/2$ converts the peak power of sine waves to the average power.

III. Problem Formulation

We characterize the R-E region through multiple current maximization problems subject to transmit power, IRS magnitude, and different rate constraints

$$\max_{\boldsymbol{\phi}, \boldsymbol{w}_I, \boldsymbol{w}_P, \rho} \quad z(\boldsymbol{\phi}, \boldsymbol{w}_I, \boldsymbol{w}_P, \rho) \quad (17a)$$

$$\text{s.t.} \quad \frac{1}{2}\left(\|\boldsymbol{w}_I\|^2 + \|\boldsymbol{w}_P\|^2\right) \leq P, \quad (17b)$$

$$R(\boldsymbol{\phi}, \boldsymbol{w}_I, \rho) \geq \bar{R}, \quad (17c)$$

$$|\phi_l| = 1, \quad l = 1, \ldots, L, \quad (17d)$$

$$0 \leq \rho \leq 1 \quad (17e)$$

Problem 17 is intricate due to coupled variables involved in non-convex objective function 17a and rate constraint 17c. To reduce the design complexity, we propose an suboptimal AO algorithm that iteratively updates the IRS phase shift and transmit waveform plus the receive splitting ratio until convergence.

A. IRS Phase Shift

In this section, the IRS phase shift $\boldsymbol{\phi}$ is optimized for any given waveform $\boldsymbol{w}_{I/P}$ and splitting ratio ρ. We observe that

$$\begin{aligned}|\boldsymbol{h}_n^H\boldsymbol{w}_{I,n}|^2 &= \boldsymbol{w}_{I,n}^H\boldsymbol{h}_n\boldsymbol{h}_n^H\boldsymbol{w}_{I,n}\\ &= \boldsymbol{w}_{I,n}^H(\boldsymbol{h}_{D,n}+\boldsymbol{V}_n^H\boldsymbol{\phi})(\boldsymbol{h}_{D,n}^H+\boldsymbol{\phi}^H\boldsymbol{V}_n)\boldsymbol{w}_{I,n}\\ &= \boldsymbol{w}_{I,n}^H\boldsymbol{M}_n^H\boldsymbol{\Phi}\boldsymbol{M}_n\boldsymbol{w}_{I,n}\\ &= \mathrm{Tr}(\boldsymbol{M}_n\boldsymbol{w}_{I,n}\boldsymbol{w}_{I,n}^H\boldsymbol{M}_n^H\boldsymbol{\Phi})\\ &= \mathrm{Tr}(\boldsymbol{C}_n\boldsymbol{\Phi})\end{aligned} \tag{18}$$

where t is an auxiliary variable with unit modulus, $\boldsymbol{M}_n = [\boldsymbol{V}_n^H, \boldsymbol{h}_{D,n}]^H \in \mathbb{C}^{(L+1)\times M}$, $\bar{\boldsymbol{\phi}} = [\boldsymbol{\phi}^H, t]^H \in \mathbb{C}^{(L+1)\times 1}$, $\boldsymbol{\Phi} = \bar{\boldsymbol{\phi}}\bar{\boldsymbol{\phi}}^H \in \mathbb{C}^{(L+1)\times(L+1)}$, $\boldsymbol{C}_n = \boldsymbol{M}_n\boldsymbol{w}_{I,n}\boldsymbol{w}_{I,n}^H\boldsymbol{M}_n^H \in \mathbb{C}^{(L+1)\times(L+1)}$. Also, define $t_{I/P,n}$ $(n = -N+1,\ldots,N-1)$ as

$$\begin{aligned}t_{I/P,n} &= \boldsymbol{h}^H\boldsymbol{W}_{I/P,n}\boldsymbol{h}\\ &= \mathrm{Tr}(\boldsymbol{h}\boldsymbol{h}^H\boldsymbol{W}_{I/P,n})\\ &= \mathrm{Tr}\left((\boldsymbol{h}_D+\boldsymbol{V}^H\boldsymbol{\phi})(\boldsymbol{h}_D^H+\boldsymbol{\phi}^H\boldsymbol{V})\boldsymbol{W}_{I/P,n}\right)\\ &= \mathrm{Tr}(\boldsymbol{M}^H\boldsymbol{\Phi}\boldsymbol{M}\boldsymbol{W}_{I/P,n})\\ &= \mathrm{Tr}(\boldsymbol{M}\boldsymbol{W}_{I/P,n}\boldsymbol{M}^H\boldsymbol{\Phi})\\ &= \mathrm{Tr}(\boldsymbol{C}_{I/P,n}\boldsymbol{\Phi})\end{aligned} \tag{19}$$

where $\boldsymbol{V} = [\boldsymbol{V}_1,\ldots,\boldsymbol{V}_N] \in \mathbb{C}^{L\times MN}$, $\boldsymbol{M} = [\boldsymbol{V}^H, \boldsymbol{h}_D]^H \in \mathbb{C}^{(L+1)\times MN}$, $\boldsymbol{C}_{I/P,n} = \boldsymbol{M}\boldsymbol{W}_{I/P,n}\boldsymbol{M}^H \in \mathbb{C}^{(L+1)\times(L+1)}$. Therefore, the rate and objective expressions rewrite as

$$R(\boldsymbol{\Phi}) = \sum_{n=1}^{N}\log_2\left(1+\frac{(1-\rho)\mathrm{Tr}(\boldsymbol{C}_n\boldsymbol{\Phi})}{\sigma_n^2}\right) \tag{20}$$

$$\begin{aligned}z(\boldsymbol{\Phi}) &= \frac{1}{2}\beta_2\rho(t_{I,0}+t_{P,0})\\ &\quad+\frac{3}{8}\beta_4\rho^2\left(2t_{I,0}^2+\sum_{n=-N+1}^{N-1}t_{P,n}t_{P,n}^*\right)\\ &\quad+\frac{3}{2}\beta_4\rho^2t_{I,0}t_{P,0}\end{aligned} \tag{21}$$

To maximize non-concave expression 21, we propose a Successive Convex Approximation (SCA) algorithm that approximate the second-order terms by first-order Taylor expansion. Based on the variables optimized at iteration $i-1$, the local approximation at iteration i suggests [45]

$$(t_{I,0}^{(i)})^2 \geq 2t_{I,0}^{(i)}t_{I,0}^{(i-1)} - (t_{I,0}^{(i-1)})^2 \tag{22}$$

$$t_{P,n}^{(i)}(t_{P,n}^{(i)})^* \geq 2\Re\left\{t_{P,n}^{(i)}(t_{P,n}^{(i-1)})^*\right\} - t_{P,n}^{(i-1)}(t_{P,n}^{(i-1)})^* \tag{23}$$

$$\begin{aligned}t_{I,0}^{(i)}t_{P,0}^{(i)} &= \frac{1}{4}(t_{I,0}^{(i)}+t_{P,0}^{(i)})^2 - \frac{1}{4}(t_{I,0}^{(i)}-t_{P,0}^{(i)})^2\\ &\geq \frac{1}{2}(t_{I,0}^{(i)}+t_{P,0}^{(i)})(t_{I,0}^{(i-1)}+t_{P,0}^{(i-1)})\\ &\quad-\frac{1}{4}(t_{I,0}^{(i-1)}+t_{P,0}^{(i-1)})^2 - \frac{1}{4}(t_{I,0}^{(i)}-t_{P,0}^{(i)})^2\end{aligned} \tag{24}$$

which provide lower bounds to the corresponding terms in 21. At iteration i, the approximated objection function $\tilde{z}(\boldsymbol{\Phi}^{(i)})$ is detailed in 25. Hence, problem 17 is transformed to

$$\max_{\boldsymbol{\Phi}} \quad \tilde{z}(\boldsymbol{\Phi}) \tag{26a}$$

$$\text{s.t.} \quad R(\boldsymbol{\Phi}) \geq \bar{R}, \tag{26b}$$

$$\boldsymbol{\Phi}_{l,l} = 1, \quad l = 1,\ldots,L+1, \tag{26c}$$

$$\boldsymbol{\Phi} \succeq 0, \tag{26d}$$

$$\mathrm{rank}(\boldsymbol{\Phi}) = 1 \tag{26e}$$

Problem 26 is not a standard Semidefinite Programming (SDP) due to the rate constraint 26b. If we relax the rank

$$z(\boldsymbol{\phi},\boldsymbol{w}_I,\boldsymbol{w}_P,\rho) = \beta_2\rho\Big(\mathcal{E}\left\{\mathcal{A}\left\{y_I^2(t)\right\}\right\} + \mathcal{A}\left\{y_P^2(t)\right\}\Big) + \beta_4\rho^2\Big(\mathcal{E}\left\{\mathcal{A}\left\{y_I^4(t)\right\}\right\} + \mathcal{A}\left\{y_P^4(t)\right\} + 6\mathcal{E}\left\{\mathcal{A}\left\{y_I^2(t)\right\}\right\}\mathcal{A}\left\{y_P^2(t)\right\}\Big) \tag{11}$$

$$\mathcal{E}\left\{\mathcal{A}\left\{y_I^2(t)\right\}\right\} = \frac{1}{2}\sum_{n=1}^{N}(\boldsymbol{h}_n^H\boldsymbol{w}_{I,n})(\boldsymbol{h}_n^H\boldsymbol{w}_{I,n})^H = \frac{1}{2}\boldsymbol{h}^H\boldsymbol{W}_{I,0}\boldsymbol{h} \tag{12}$$

$$\mathcal{E}\left\{\mathcal{A}\left\{y_I^4(t)\right\}\right\} = \frac{3}{4}\left(\sum_{n=1}^{N}(\boldsymbol{h}_n^H\boldsymbol{w}_{I,n})(\boldsymbol{h}_n^H\boldsymbol{w}_{I,n})^H\right)^2 = \frac{3}{4}(\boldsymbol{h}^H\boldsymbol{W}_{I,0}\boldsymbol{h})^2 \tag{13}$$

$$\mathcal{A}\left\{y_P^2(t)\right\} = \frac{1}{2}\sum_{n=1}^{N}(\boldsymbol{h}_n^H\boldsymbol{w}_{P,n})(\boldsymbol{h}_n^H\boldsymbol{w}_{P,n})^H = \frac{1}{2}\boldsymbol{h}^H\boldsymbol{W}_{P,0}\boldsymbol{h} \tag{14}$$

$$\mathcal{A}\left\{y_P^4(t)\right\} = \frac{3}{8}\sum_{\substack{n_1,n_2,n_3,n_4\\ n_1+n_2=n_3+n_4}}(\boldsymbol{h}_{n_1}^H\boldsymbol{w}_{P,n_1})(\boldsymbol{h}_{n_2}^H\boldsymbol{w}_{P,n_2})(\boldsymbol{h}_{n_3}^H\boldsymbol{w}_{P,n_3})^H(\boldsymbol{h}_{n_4}^H\boldsymbol{w}_{P,n_4})^H = \frac{3}{8}\sum_{n=-N+1}^{N-1}(\boldsymbol{h}^H\boldsymbol{W}_{P,n}\boldsymbol{h})(\boldsymbol{h}^H\boldsymbol{W}_{P,n}\boldsymbol{h})^H \tag{15}$$

Algorithm 1 SCA: IRS Phase Shift

input $\beta_2, \beta_4, \boldsymbol{h}_{D,n}, \boldsymbol{H}_{I,n}, \boldsymbol{h}_{R,n}, \boldsymbol{w}_I, \boldsymbol{w}_P, \rho, \sigma_n, \bar{R}, Q, \epsilon$
Construct $\boldsymbol{M}, \boldsymbol{M}_n, \boldsymbol{C}_n$ for $n = 1, \ldots, N$, $\boldsymbol{C}_{I/P,n}$ for $n = -N+1, \ldots, N-1$
initialize $i \leftarrow 0, \boldsymbol{\Phi}^{(0)}, t_{I/P,n}^{(0)}$ for $n = -N+1, \ldots, N-1$
repeat
  $i \leftarrow i+1$
  Obtain $\boldsymbol{\Phi}^{(i)}, t_{I/P,n}^{(i)}$ by solving problem 26
  Compute $z^{(i)}$ by 21
until $|z^{(i)} - z^{(i-1)}| \leq \epsilon$
Set $\boldsymbol{\Phi}^\star = \boldsymbol{\Phi}^{(i)}$
if $\mathrm{rank}(\boldsymbol{\Phi}^\star) = 1$ **then**
  Obtain $\bar{\boldsymbol{\phi}}^\star$ by EVD, $\boldsymbol{\Phi}^\star = \bar{\boldsymbol{\phi}}^\star (\bar{\boldsymbol{\phi}}^\star)^H$
else
  Obtain $\boldsymbol{U}, \boldsymbol{\Sigma}$ by EVD, $\boldsymbol{\Phi}^\star = \boldsymbol{U}\boldsymbol{\Sigma}\boldsymbol{U}^H$
  Generate $\boldsymbol{r}_q \sim \mathcal{CN}(\boldsymbol{0}, \boldsymbol{I}_{L+1})$, $q = 1, \ldots, Q$
  Construct $\bar{\boldsymbol{\phi}}_q = e^{j \arg\left(\boldsymbol{U}\boldsymbol{\Sigma}^{1/2}\boldsymbol{r}_q\right)}$, $\boldsymbol{\Phi}_q = \bar{\boldsymbol{\phi}}_q \bar{\boldsymbol{\phi}}_q^H$
  Set $q^\star = \arg\max_q z(\boldsymbol{\Phi}_q)$, $\bar{\boldsymbol{\phi}}^\star = \bar{\boldsymbol{\phi}}_{q^\star}$
end if
Set $\theta_l^\star = \arg(\phi_l^\star / \phi_{L+1}^\star),\ l = 1, \ldots, L$, construct $\boldsymbol{\phi}^\star$
output $\boldsymbol{\phi}^\star$

constraint 26e to formulate a convex problem, there is no guarantee that the optimal rank-1 solution $\bar{\boldsymbol{\phi}}^\star$ extracted from $\boldsymbol{\Phi}^\star$ is a stationary point of the original problem 17. In Section IV, we numerically show that $\boldsymbol{\Phi}^\star$ is rank-1 for all tested channel realizations so that the performance loss is insignificant. A related version of problem 26 can be solved using existing optimization tools such as CVX [46].

When $\boldsymbol{\Phi}^\star$ is rank-1, the optimal phase shift vector $\bar{\boldsymbol{\phi}}^\star$ can be obtained by Eigenvalue Decomposition (EVD). Otherwise, a suboptimal solution can be extracted via Gaussian randomization method [47]. Specifically, we perform EVD $\boldsymbol{\Phi}^\star = \boldsymbol{U}\boldsymbol{\Sigma}\boldsymbol{U}^H$, generate Q CSCG random vectors $\boldsymbol{r}_q \sim \mathcal{CN}(\boldsymbol{0}, \boldsymbol{I}_{L+1}),\ q = 1, \ldots, Q$, construct the corresponding candidates $\bar{\boldsymbol{\phi}}_q = e^{j \arg\left(\boldsymbol{U}\boldsymbol{\Sigma}^{1/2}\boldsymbol{r}_q\right)}$, and choose the one that maximizes the objective function 26a. Finally, the phase shift is retrieved by $\theta_l = \arg(\phi_l^\star / \phi_{L+1}^\star),\ l = 1, \ldots, L$. The algorithm for phase shift optimization is summarized in Algorithm 1.

B. Waveform and Splitting Ratio

Next, we jointly optimize both information and power waveforms $\boldsymbol{w}_{I/P}$ together with splitting ratio ρ for any given IRS phase shift $\boldsymbol{\phi}$. As pointed out in [40], the waveform design in frequency and spatial domain can be decoupled without performance loss, and the optimal spatial weight is given by Maximum-Ratio Transmission (MRT) beamformer

$$\boldsymbol{w}_{I/P,n} = s_{I/P,n} \frac{\boldsymbol{h}_n}{\|\boldsymbol{h}_n\|} \tag{27}$$

That is to say, for single-user MISO SWIPT, it is only necessary to determine the amplitudes $s_{I/P,n}$ at different tones. Hence, the original waveform optimization with $2MN$ complex variables is converted into a power allocation problem with $2N$ nonnegative real variables. Let $\boldsymbol{s}_{I/P} = [s_{I/P,1}, \ldots, s_{I/P,N}]^T \in \mathbb{C}^{N \times 1}$. At subband n, the effective channel gain is given by $\|\boldsymbol{h}_n\|$, and the power allocated to the modulated and unmodulated waveform are given by $s_{I,n}^2$ and $s_{P,n}^2$, respectively. With such an active beamformer selection, we have $\boldsymbol{h}_n^H \boldsymbol{w}_{I,n} = |\boldsymbol{h}_n^H \boldsymbol{w}_{I,n}| = \|\boldsymbol{h}_n\| s_{I,n}$ such that the rate and objective expressions further reduces to 28 and 29.

$$R(\boldsymbol{s}_I, \rho) = \log_2 \left(\prod_{n=1}^{N} \left(1 + \frac{(1-\rho)\|\boldsymbol{h}_n\|^2 s_{I,n}^2}{\sigma_n^2} \right) \right) \tag{28}$$

Therefore, problem 17 is reduced to an amplitude optimization issue

$$\max_{\boldsymbol{s}_I, \boldsymbol{s}_P, \rho} \quad z(\boldsymbol{s}_I, \boldsymbol{s}_P, \rho) \tag{30a}$$

$$\text{s.t.} \quad \frac{1}{2}\left(\|\boldsymbol{s}_I\|^2 + \|\boldsymbol{s}_P\|^2\right) \leq P, \tag{30b}$$

$$R(\boldsymbol{s}_I, \rho) \geq \bar{R} \tag{30c}$$

Since problem 30 involves the production of nonnegative real variables, we introduce auxiliary variables $t', \bar{\rho}$ and transform it into a reversed GP

$$\min_{\boldsymbol{s}_I, \boldsymbol{s}_P, \rho, \bar{\rho}, t'} \quad \frac{1}{t'} \tag{31a}$$

$$\text{s.t.} \quad \frac{1}{2}\left(\|\boldsymbol{s}_I\|^2 + \|\boldsymbol{s}_P\|^2\right) \leq P, \tag{31b}$$

$$\frac{t'}{z(\boldsymbol{s}_I, \boldsymbol{s}_P, \rho)} \leq 1, \tag{31c}$$

$$\frac{2^{\bar{R}}}{\prod_{n=1}^{N}\left(1 + \bar{\rho}\|\boldsymbol{h}_n\|^2 s_{I,n}^2 / \sigma_n^2\right)} \leq 1, \tag{31d}$$

$$\rho + \bar{\rho} \leq 1 \tag{31e}$$

The denominators of 31c, 31d are posynomials [48], and we further rewrite them as

$$z(\boldsymbol{s}_I, \boldsymbol{s}_P, \rho) = \sum_{m_P} g_{m_P}(\boldsymbol{s}_I, \boldsymbol{s}_P, \rho) \tag{32}$$

$$1 + \frac{\bar{\rho}\|\boldsymbol{h}_n\|^2 s_{I,n}^2}{\sigma_n^2} = \sum_{m_{I,n}} g_{m_{I,n}}(s_{I,n}, \bar{\rho}) \tag{33}$$

$$\begin{aligned}
\tilde{z}(\boldsymbol{\Phi}^{(i)}) = {} & \frac{1}{2}\beta_2 \rho (t_{I,0}^{(i)} + t_{P,0}^{(i)}) \\
& + \frac{3}{8}\beta_4 \rho^2 \left(4(t_{I,0}^{(i)})(t_{I,0}^{(i-1)}) - 2(t_{I,0}^{(i-1)})^2 + \sum_{n=-N+1}^{N-1} 2\Re\left\{ t_{P,n}^{(i)} (t_{P,n}^{(i-1)})^* \right\} - t_{P,n}^{(i-1)} (t_{P,n}^{(i-1)})^* \right) \\
& + \frac{3}{2}\beta_4 \rho^2 \left(\frac{1}{2}(t_{I,0}^{(i)} + t_{P,0}^{(i)})(t_{I,0}^{(i-1)} + t_{P,0}^{(i-1)}) - \frac{1}{4}(t_{I,0}^{(i-1)} + t_{P,0}^{(i-1)})^2 - \frac{1}{4}(t_{I,0}^{(i)} - t_{P,0}^{(i)})^2 \right)
\end{aligned} \tag{25}$$

where $m_P, m_{I,n}$ are the number of monomials in the corresponding posynomials (obviously $m_{I,n} = 2$). Following [40], [49], we upper bound posynomials 32 and 33 by Arithmetic Mean-Geometric Mean (AM-GM) inequality such that problem 31 reduces to

$$\min_{\boldsymbol{s}_I, \boldsymbol{s}_P, \rho, \bar{\rho}, t'} \quad \frac{1}{t'} \tag{34a}$$

$$\text{s.t.} \quad \frac{1}{2}\left(\|\boldsymbol{s}_I\|^2 + \|\boldsymbol{s}_P\|^2\right) \le P, \tag{34b}$$

$$t' \prod_{m_P} \left(\frac{g_{m_P}(\boldsymbol{s}_I, \boldsymbol{s}_P, \rho)}{\gamma_{m_P}}\right)^{-\gamma_{m_P}} \le 1, \tag{34c}$$

$$2^{\bar{R}} \prod_{n} \prod_{m_{I,n}} \left(\frac{g_{m_{I,n}}(s_{I,n}, \bar{\rho})}{\gamma_{m_{I,n}}}\right)^{-\gamma_{m_{I,n}}} \le 1, \tag{34d}$$

$$\rho + \bar{\rho} \le 1 \tag{34e}$$

where $\gamma_{m_P}, \gamma_{m_{I,n}} \ge 0$, $\sum_{m_P} \gamma_{m_P} = \sum_{m_{I,n}} \gamma_{m_{I,n}} = 1$. The tightness of the AM-GM inequality depends on $\{\gamma_{m_P}, \gamma_{m_{I,n}}\}$ that require successive update. As suggested in [40], a feasible choice at iteration i is

$$\gamma_{m_P}^{(i)} = \frac{g_{m_P}(\boldsymbol{s}_I^{(i-1)}, \boldsymbol{s}_P^{(i-1)}, \rho^{(i-1)})}{z(\boldsymbol{s}_I^{(i-1)}, \boldsymbol{s}_P^{(i-1)}, \rho^{(i-1)})} \tag{35}$$

$$\gamma_{m_{I,n}}^{(i)} = \frac{g_{m_{I,n}}(s_{I,n}^{(i-1)}, \bar{\rho}^{(i-1)})}{1 + \bar{\rho}^{(i-1)}\|\boldsymbol{h}_n\|^2 (s_{I,n}^{(i-1)})^2/\sigma_n^2} \tag{36}$$

Problem 34 can be solved using existing optimization tools such as CVX [46]. $\boldsymbol{s}_I, \boldsymbol{s}_P, \rho$ are updated iteratively until convergence. The GP algorithm is summarized in Algorithm 2.

C. Alternating Optimization

For any direct, incident and reflective channels, we iteratively update the IRS phase shift by Algorithm 1 and update the transmit waveform with receive splitting ratio by Algorithm 2 until convergence. The alternating algorithm is summarized in Algorithm 3.

D. Convergence

The proposed alternating algorithm iteratively employs SCA-based IRS phase shift Algorithm 1 and GP-based waveform and splitting ratio Algorithm 2 until convergence.

Algorithm 2 GP: Waveform and Splitting Ratio

1: **Input** $\beta_2, \beta_4, \boldsymbol{h}, P, \sigma_n, \bar{R}, \epsilon$
2: **Initialize** $i \leftarrow 0$, $\boldsymbol{s}_{I/P}^{(0)}$, $\rho^{(0)}$
3: **repeat**
4: $\quad i \leftarrow i + 1$
5: $\quad$ Update $\{\gamma_{m_P}^{(i)}, \gamma_{m_{I,n}}^{(i)}\}$ by 35, 36
6: $\quad$ Obtain $\boldsymbol{s}_{I/P}^{(i)}, \rho^{(i)}$ by solving problem 34
7: $\quad$ Compute $z^{(i)}$ by 29
8: **until** $|z^{(i)} - z^{(i-1)}| \le \epsilon$
9: Set $\boldsymbol{s}_{I/P}^{\star} = \boldsymbol{s}_{I/P}^{(i)}$, $\rho^{\star} = \rho^{(i)}$, retrieve $\boldsymbol{w}_{I/P}^{\star}$ by 27
10: **Output** $\boldsymbol{w}_{I/P}^{\star}, \rho^{\star}$

Algorithm 3 AO: Waveform, Active and Passive Beamforming

1: **Input** $\beta_2, \beta_4, \boldsymbol{h}_{D,n}, \boldsymbol{H}_{I,n}, \boldsymbol{h}_{R,n}, P, \sigma_n, \bar{R}, Q, \epsilon$
2: **Initialize** $i \leftarrow 0$, $\boldsymbol{\phi}^{(0)}, \boldsymbol{w}_{I/P}^{(0)}, \rho^{(0)}$
3: **repeat**
4: $\quad i \leftarrow i + 1$
5: $\quad$ Fix $\boldsymbol{w}_{I/P}^{(i-1)}, \rho^{(i-1)}$ and obtain $\boldsymbol{\phi}^{(i)}$ by Algorithm 1
6: $\quad$ Fix $\boldsymbol{\phi}^{(i)}$, update $\boldsymbol{h}_n^{(i)}$ by 4, and obtain $\boldsymbol{w}_{I/P}^{(i)}, \rho^{(i)}$ by Algorithm 2
7: $\quad$ Compute $z^{(i)}$ by 21
8: **until** $|z^{(i)} - z^{(i-1)}| \le \epsilon$
9: **Output** $\boldsymbol{\phi}^{\star}, \boldsymbol{w}_{I/P}^{\star}, \rho^{\star}$

Proposition 1. *For any feasible initial point, the proposed SCA-based Algorithm 1 is guaranteed to converge to a stationary point of the IRS phase shift subproblem.*

Proof. The objective function 26a is non-decreasing over iterations because the solution of problem 26 at iteration $i-1$ is still a feasible point at iteration i. Moreover, the sequence $\{\tilde{z}(\boldsymbol{\Phi}^{(i)})\}_{i=1}^{\infty}$ is bounded above due to the unit-modulus constraint 26c. Thus, Algorithm 1 is guaranteed to converge. To prove $\boldsymbol{\Phi}^{(i)}$ converge to the set of stationary points of IRS subproblem, we notice that the SCA-based Algorithm 1 is indeed an inner approximation algorithm [50], since $\tilde{z}(\boldsymbol{\Phi}) \le z(\boldsymbol{\Phi})$, $\partial\tilde{z}(\boldsymbol{\Phi}^{(i)})/\partial\boldsymbol{\Phi} = \partial z(\boldsymbol{\Phi}^{(i)})/\partial\boldsymbol{\Phi}$ and the approximation 22 – 24 are asymptotically tight as $i \to \infty$ [45], [51]. Therefore, Algorithm 1 converges to a stationary point. □

Proposition 2. *For any feasible initial point, the GP-based Algorithm 2 is guaranteed to converge to a stationary point of*

$$\begin{aligned} z(\boldsymbol{s}_I, \boldsymbol{s}_P, \rho) = {} & \frac{1}{2}\beta_2\rho \sum_{n=1}^{N} \|\boldsymbol{h}_n\|^2 (s_{I,n}^2 + s_{P,n}^2) \\ & + \frac{3}{8}\beta_4\rho^2 \left(2 \sum_{n_1,n_2} \prod_{j=1}^{2} \|\boldsymbol{h}_{n_j}\|^2 s_{I,n_j}^2 + \sum_{\substack{n_1,n_2,n_3,n_4 \\ n_1+n_2=n_3+n_4}} \prod_{j=1}^{4} \|\boldsymbol{h}_{n_j}\| s_{P,n_j}\right) \\ & + \frac{3}{2}\beta_4\rho^2 \left(\sum_{n_1,n_2} \|\boldsymbol{h}_{n_1}\|^2 s_{I,n_1}^2 \|\boldsymbol{h}_{n_2}\|^2 s_{P,n_2}^2\right) \end{aligned} \tag{29}$$

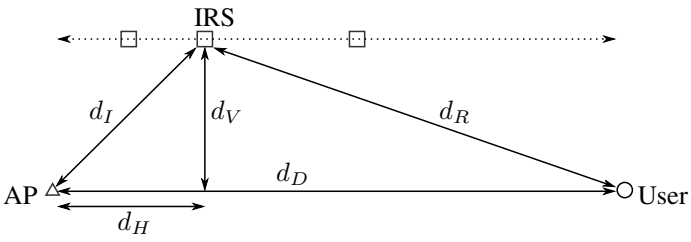

Fig. 3. System layout

the waveform and splitting ratio subproblem.

Proof. See [10], [40]. □

Proposition 3. *Every limit point* $(\boldsymbol{\phi}^\star, \boldsymbol{w}_I^\star, \boldsymbol{w}_P^\star, \rho^\star)$ *of the proposed alternating algorithm is a stationary point of the original problem 17.*

Proof. The objective function 17a is non-decreasing over iterations of Algorithm 3, which is also upper-bounded due to the unit-modulus constraint 17d and the average transmit power constraint 17b. Thus, Algorithm 3 is guaranteed to converge, namely the sequence $\{\boldsymbol{\phi}^{(i)}, \boldsymbol{w}_I^{(i)}, \boldsymbol{w}_P^{(i)}, \rho^{(i)}\}$ generated by optimizing $\boldsymbol{\phi}$ and $\boldsymbol{w}_I, \boldsymbol{w}_P, \rho$ alternatively has limit points. As demonstrated in [52]–[54], the solution is a stationary point of problem 17. □

IV. Performance Evaluations

To evaluate the performance of the proposed IRS-aided SWIPT system, we characterize the average R-E regions under typical setups. Consider a large open space WiFi-like environment at a center frequency of 5.18 GHz with reference bandwidth $B = 1\,\text{MHz}$. As shown in Fig. 3, we assume the IRS moves along a horizontal line parallel to the AP-user path and let d_H, d_V be the horizontal and vertical distances from the AP to the IRS, respectively. We also denote d_D, d_I, d_R as the length of direct, incident, reflective paths such that $d_I = \sqrt{d_H^2 + d_V^2}$, $d_R = \sqrt{(d_D - d_H)^2 + d_V^2}$, and choose $d_D = 15\,\text{m}$, $d_V = 2\,\text{m}$ and reference $d_H = 2\,\text{m}$. The path loss and fading parameters are obtained from IEEE TGn channel model D [55]. Reference path loss is set to $L_0 = -35\,\text{dB}$ at $d_0 = 1\,\text{m}$. For NLoS channels, all taps are modelled as i.i.d. CSCG random variables. For LoS channels, the first tap, whose power is significantly larger, is in circular uniform distribution while the remaining taps are in i.i.d. CSCG distribution. The average sum-power of all taps is unit such that the multipath response is normalized. All channels are regarded as NLoS unless otherwise mentioned. We choose number of transmit antennas $M = 1$, number of reflectors $L = 20$, number of subbands $N = 16$ as reference, and assume no spatial correlation across all elements. Rectenna parameters are taken as $k_2 = 0.0034$, $k_4 = 0.3829$, $R_{\text{ant}} = 50\,\Omega$. With $0\,\text{dBi}$ transmit antenna gain, the average Effective Isotropic Radiated Power (EIRP) is fixed to $MP = -36\,\text{dBm}$ while the reference average noise power is $\sigma_n = -40\,\text{dBm}$ at all subbands. We also assume $0\,\text{dBi}$ IRS element gain and $2\,\text{dBi}$ receive antenna gain. For the algorithm, the tolerance is $\epsilon = 10^{-8}$, the number of candidates in the Gaussian randomization method is $Q = 10^3$,

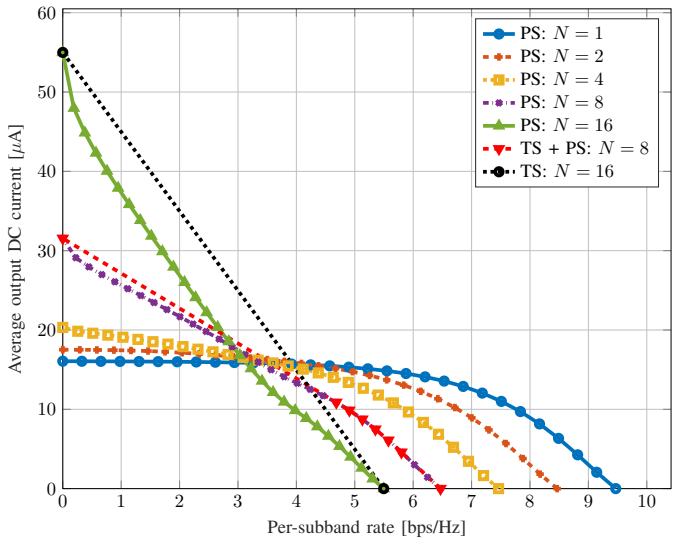

Fig. 4. Average R-E region versus the number of subbands

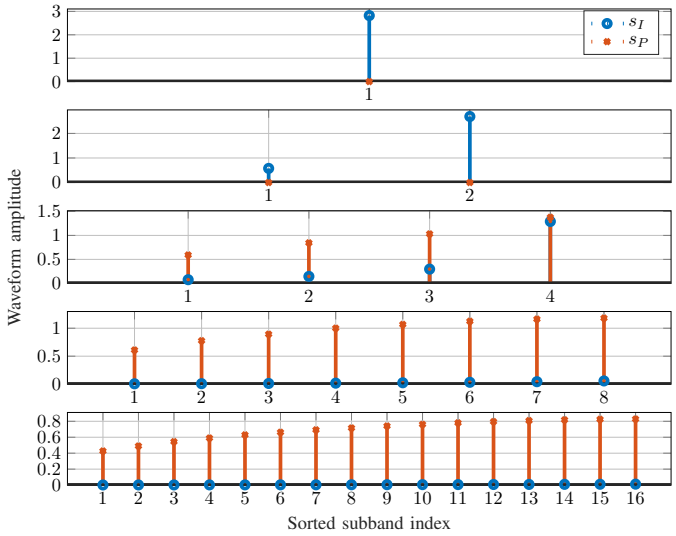

Fig. 5. Sorted waveform amplitude versus the number of subbands

and the R-E region is averaged over 200 channel realizations. In the R-E boundary, the leftmost point corresponds to WPT ($\rho = 1$) where power can be allocated simultaneously to modulated and unmodulated waveform to maximize the average output DC current. On the other hand, the rightmost point corresponds to WIT ($\rho = 0$) where the solution coincides with the Water-Filling (WF) algorithm that allocates all power to modulated waveform only. For a fair comparison, the x-axis of the plots has been normalized to per-subband rate.

We first evaluate the performance of Algorithm 1 under SDR. It is demonstrated that $\boldsymbol{\Theta}^\star$ is rank-1 for all tested channel realizations with different M, N and L. Therefore, $\boldsymbol{\theta}^\star$ can be directly obtained through EVD and we claim Algorithm 1 converges to stationary points of problem 26 without performance loss.

Fig. 4 illustrates the average R-E region versus the number of subband N. *First*, it is observed that increasing N reduces the

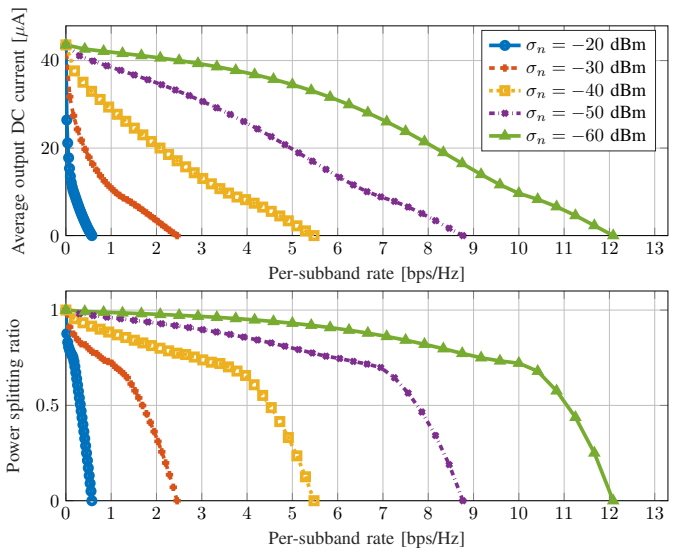

Fig. 6. Average R-E region and splitting ratio versus the average noise power

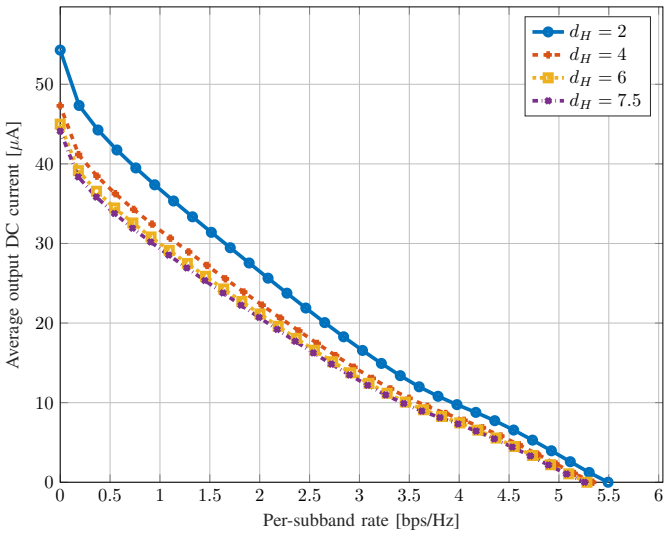

Fig. 7. Average R-E region versus AP-IRS horizontal distance

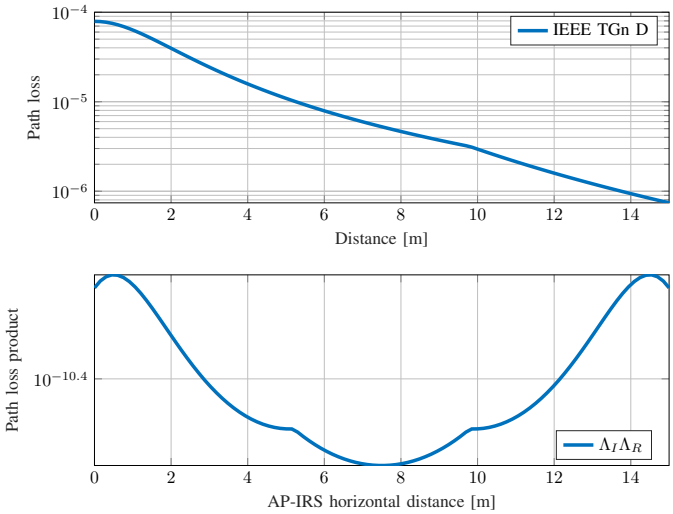

Fig. 8. Path loss versus distance

per-subband rate but boosts the harvested energy. The reason is that although each subband receives a smaller proportion of the total power, more balanced terms are introduced to further amplify the output DC current, as suggested by the scaling laws in [40]. Waveform amplitude in Fig. 5 also confirmed that from the perspective of WPT, dedicated multisine waveform is unnecessary for a small N but is required for a large N. As shown in 13 and 15, the only difference of modulated and unmodulated waveform on z exists in the fourth-order terms, where $\mathcal{E}\left\{\mathcal{A}\left\{y_I^4(t)\right\}\right\}$ has N^2 monomials with a modulation gain of 2 and $\mathcal{A}\left\{y_P^4(t)\right\}$ has $(2N^3+N)/3$ monomials without modulation gain. Therefore, superposed waveform enlarges the R-E region for a sufficiently large N (typically no smaller than 4). However, an excessively large N not only increases computation complexity but also operates out of the small-signal harvester model, thus become prohibitive. *Second*, the R-E region is convex for $N = 2, 4$ and concave-convex for $N = 8, 16$. This has the consequence that PS outperforms TS for a small N and is outperformed for a large N. When N is in between, the optimal strategy is a combination of both, i.e. a time sharing between the WPT point and the tangent WIPT point obtained by PS. Compared with the linear harvester model that requires no dedicated power waveform and always prefer PS, the rectifier nonlinearity enlarges the R-E region by favouring a different waveform and transceiving strategy, both heavily depends on N.

The influence of the average noise power on the average R-E region is investigated in Fig. 6. We *first* note that for a large number of subbands ($N = 16$), the R-E region is approximately concave for a high noise level and approximately convex for a low noise level. Hence, TS is preferred at low SNR while PS is preferred at high SNR. This is because at a low SNR, the capacity-achieving WF algorithm tends to allocate more power to few strongest subbands. As the rate constraint $\bar{R}$ decreases, more subbands are activated to further boost the harvested energy via the coupling effect by rectifier nonlinearity. *Second*, there exists a turning point in the R-E region especially for a small noise ($\sigma_n \leq -40\,\mathrm{dBm}$). The reason is that when $\bar{R}$ departs slightly from the capacity, the algorithm mainly adjusts the splitting ratio ρ rather than put more weight on the multisine waveform, since a small amplitude could be inefficient for energy maximization. On the other hand, as $\bar{R}$ further reduces, a modulated waveform with a very large ρ could be outperformed by a superposed waveform with a smaller ρ, due to advantage the of multisine. The result highlights the necessity of joint optimization of waveform and splitting ratio.

In Fig. 7, we compare the average R-E region achieved by different AP-IRS horizontal distance d_H. A *first* observation is that, different from the active relay that prefers the middle point, placing the IRS closer to either the AP or the user would further improve the R-E tradeoff. It origins from the product-distance path loss model that applies to finite-size element reflection. As shown in Fig. 8, although the piecewise TGn path loss model further penalizes large distance (greater than

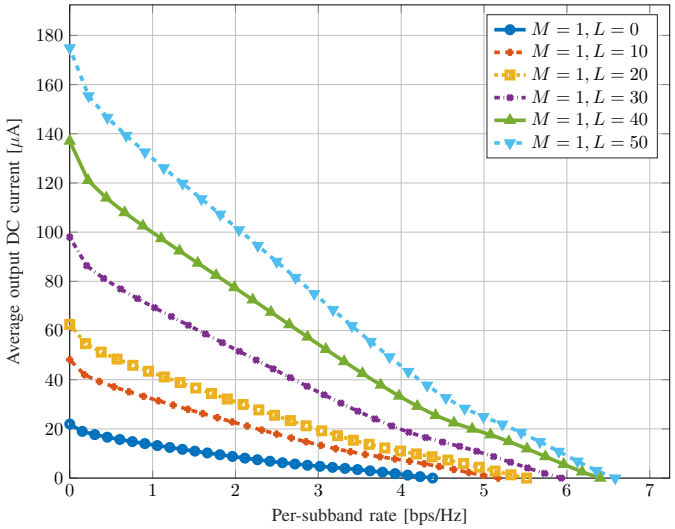

Fig. 9. Average R-E region versus the number of reflectors

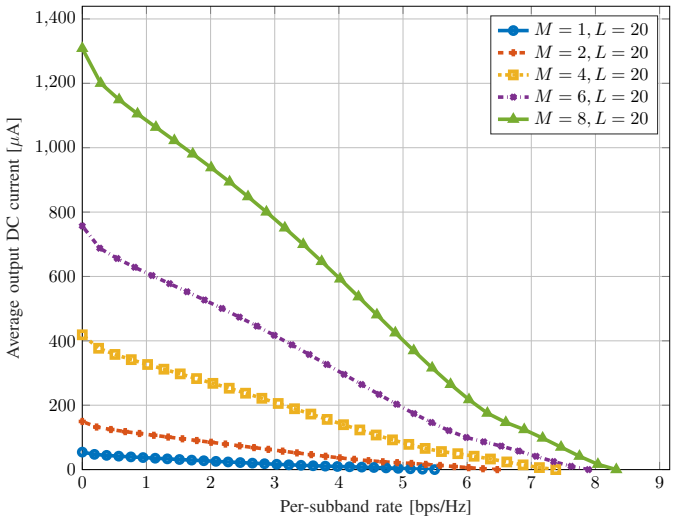

Fig. 10. Average R-E region versus the number of transmit antennas

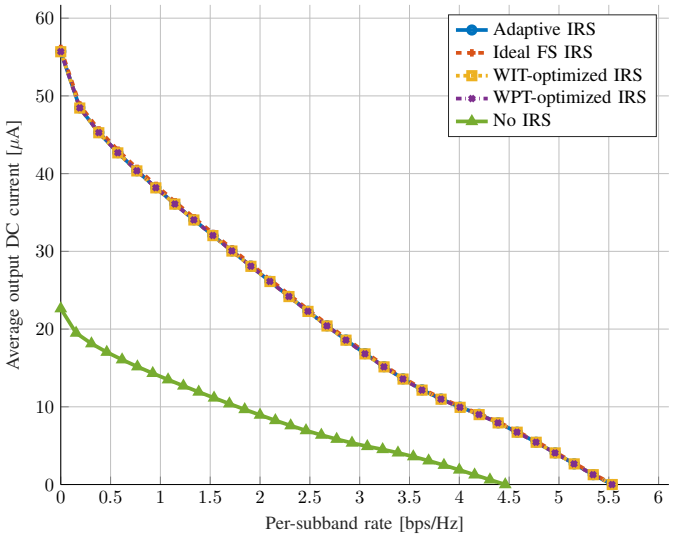

Fig. 11. Average R-E region for adaptive, ideal, fixed and no IRS over $B = 1\,\mathrm{MHz}$

$10\,\mathrm{m}$ for model D), it is still beneficial to have a short-long or long-short transmission setup, since signal attenuation increases fast at a short distance and experiences marginal effect at a long distance. On the other hand, it also suggests that developing an IRS next to the AP can effectively extend the operation range of SWIPT systems. Considering the passive characteristic of IRS, opportunities are that it can be directly supported by the SWIPT network. A *second* observation is that there exists two optimal IRS development locations that maximizes the path loss production $\Lambda_I \Lambda_R$. It implies that more than one IRS may be implemented to further enlarge the R-E region, one attached to the AP and one attached to the IRS.

The impact of the number of transmit antennas M and IRS reflectors L on the average R-E tradeoff is revealed in Fig. 9 and 10. A *first* contrast indicates that adding either active or passive elements benefits both information and power transmission while preserving the concavity-convexity of the R-E region. This is because increasing M or L indeed enhances the equivalent composite channel strength such that the magnitude of the components in 11 is amplified while the amount remains unchanged. Therefore, we conclude that number of transmit antennas and reflectors have basically no influence on the waveform preference and transceiving strategy. A *second* contrast suggests that the system performance is more sensitive to the variation of M, compared with L. Interestingly, the active MRT beamformer only has a transmit array gain of M. In contrast, the IRS collects L signal copies with a receive array gain L, then performs an equal gain reflection with a reflect array gain L, achieving a total array gain of L^2. However, the system performance in our setup is dominated by the direct link. As shown in Fig. 8, the direct path loss Λ_D is in the scope of 10^{-7} while the extra path loss product $\Lambda_I \Lambda_R$ is below 10^{-10}. This has the consequence that despite increasing L can effectively enhance the AP-IRS-user extra channel, its amplitude is still too small compared with the AP-user channel such that increasing M is more effective to improve the system performance.

Fig. 11 and 12 explore the average R-E region under different IRS configuration for narrowband transmission ($B = 1\,\mathrm{MHz}$) and broadband transmission ($B = 10\,\mathrm{MHz}$). The adaptive scheme optimizes the IRS and waveform alternatively for each points in the R-E boundary. In comparison, the WIT/WPT-based schemes only perform alternating optimization for the right-most/left-most points, then fix the IRS and update the waveform to obtain the R-E curve. To gain some insight into the IRS behavior, we compare the results above to that of no IRS and the ideal FS IRS, where we assume each element has independent and adjustable reflection coefficients over all subbands such that the ideal IRS has a total DoF of NL. Since the IRS only adapts the phase of the extra channel, the optimal strategy for each FS reflector in the SISO case would be aligning the AP-IRS-user and AP-user channel over all subbands, namely

$$\theta_{l,n}^{\star} = e^{j \arg\left(h_{D,n}/(h_{I,n,l} h_{R,n,l})\right)} \tag{37}$$

First, it is observed that the presence of IRS effectively

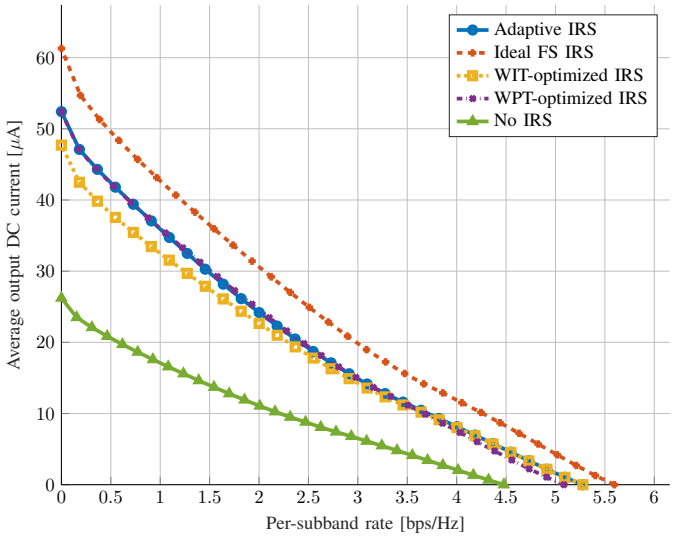

Fig. 12. Average R-E region for adaptive, ideal, fixed and no IRS over $B = 10\,\text{MHz}$

enlarges the achievable R-E region in both cases. This is because the IRS tweaks the weak extra channels such that they add constructively to enhance the composite channel. *Second*, the performance gaps of the adaptive, ideal and fixed IRS are negligible for narrowband transmission but noticeable for broadband transmission. The reason is that when $B = 1\,\text{MHz}$, all channels are approximately flat and the response of all subbands are roughly the same. In such cases, the additional DoF provided by the frequency selectivity of the ideal IRS would be unnecessary as the the optimal reflection coefficients of each element would almost align at all subbands. Similarly, WIT-optimized and WPT-optimized IRS boil down to optimizing a single term representing the composite channel response at all subbands. Therefore, all IRS strategies coincide with each other, and the optimal IRS for narrowband SISO SWIPT can be approximated by any candidate that roughly align the AP-IRS-user channel with the AP-user channel simultaneously over all subbands. On the other hand, the channel frequency selectivity becomes significant for $B = 10\,\text{MHz}$, and the ideal FS IRS outperforms the others as it requires no tradeoff among subchannels. Moreover, the WIT-optimized IRS tends to equalize the channel strength for all subbands as possible, due to the preference of WF strategy at high SNR. In comparison, the WPT-optimized IRS beams less towards few weakest subchannels, due to the inefficiency of small-amplitude tones in energy harvesting. Therefore, the adaptive IRS design is more suitable for broadband SWIPT. Note that the tradeoff for practical IRS indeed origins from frequency selectivity rather than number of subbands.

REFERENCES

[1] D. W. K. Ng, T. Q. Duong, C. Zhong, and R. Schober, Eds., *Wireless Information and Power Transfer*. Chichester, UK: John Wiley & Sons, Ltd, dec 2018. [Online]. Available: http://doi.wiley.com/10.1002/9781119476863

[2] L. R. Varshney, "Transporting information and energy simultaneously," *IEEE International Symposium on Information Theory - Proceedings*, pp. 1612–1616, 2008.

[3] X. Zhou, R. Zhang, and C. K. Ho, "Wireless information and power transfer: Architecture design and rate-energy tradeoff," *IEEE Transactions on Communications*, vol. 61, no. 11, pp. 4754–4767, 2013.

[4] R. Zhang and C. K. Ho, "MIMO broadcasting for simultaneous wireless information and power transfer," *IEEE Transactions on Wireless Communications*, vol. 12, no. 5, pp. 1989–2001, 2013.

[5] J. Xu, L. Liu, and R. Zhang, "Multiuser miso beamforming for simultaneous wireless information and power transfer," *IEEE Transactions on Signal Processing*, vol. 62, no. 18, pp. 4798–4810, 2014.

[6] I. Krikidis, S. Timotheou, S. Nikolaou, G. Zheng, D. W. K. Ng, and R. Schober, "Simultaneous Wireless Information and Power Transfer in modern communication systems," *IEEE Communications Magazine*, vol. 52, no. 11, pp. 104–110, 2014.

[7] E. Boshkovska, D. W. K. Ng, N. Zlatanov, and R. Schober, "Practical non-linear energy harvesting model and resource allocation for SWIPT systems," *IEEE Communications Letters*, vol. 19, no. 12, pp. 2082–2085, 2015.

[8] M. S. Trotter, J. D. Griffin, and G. D. Durgin, "Power-optimized waveforms for improving the range and reliability of RFID systems," *2009 IEEE International Conference on RFID, RFID 2009*, pp. 80–87, 2009.

[9] A. S. Boaventura and N. B. Carvalho, "Maximizing DC power in energy harvesting circuits using multisine excitation," *IEEE MTT-S International Microwave Symposium Digest*, vol. 1, no. 1, pp. 1–4, 2011.

[10] B. Clerckx and E. Bayguzina, "Waveform Design for Wireless Power Transfer," *IEEE Transactions on Signal Processing*, vol. 64, no. 23, pp. 6313–6328, 2016.

[11] J. Kim, B. Clerckx, and P. D. Mitcheson, "Experimental Analysis of Harvested Energy and Throughput Trade-off in a Realistic SWIPT System," 2019. [Online]. Available: http://arxiv.org/abs/1908.08272

[12] ——, "Signal and System Design for Wireless Power Transfer : Prototype, Experiment and Validation," pp. 1–31, 2019. [Online]. Available: http://arxiv.org/abs/1901.01156

[13] B. Clerckx and J. Kim, "On the Beneficial Roles of Fading and Transmit Diversity in Wireless Power Transfer with Nonlinear Energy Harvesting," *IEEE Transactions on Wireless Communications*, vol. 17, no. 11, pp. 7731–7743, 2018.

[14] J. J. Park, J. H. Moon, K. Y. Lee, and D. I. Kim, "Dual Mode SWIPT: Waveform Design and Transceiver Architecture with Adaptive Mode Switching Policy," *IEEE Vehicular Technology Conference*, vol. 2018-June, pp. 1–5, 2018.

[15] J. Hu, Y. Zhao, and K. Yang, "Modulation and Coding Design for Simultaneous Wireless Information and Power Transfer," *IEEE Communications Magazine*, vol. 57, no. 5, pp. 124–130, 2019.

[16] M. Varasteh, E. Piovano, and B. Clerckx, "A Learning Approach to Wireless Information and Power Transfer Signal and System Design," in *ICASSP 2019 - 2019 IEEE International Conference on Acoustics, Speech and Signal Processing (ICASSP)*. IEEE, may 2019, pp. 4534–4538. [Online]. Available: https://ieeexplore.ieee.org/document/8682485/

[17] Y. Liu, Z. Ding, M. Elkashlan, and H. V. Poor, "Cooperative Non-orthogonal Multiple Access with Simultaneous Wireless Information and Power Transfer," *IEEE Journal on Selected Areas in Communications*, vol. 34, no. 4, pp. 938–953, 2016.

[18] Y. Mao, B. Clerckx, and V. O. Li, "Rate-Splitting for Multi-User Multi-Antenna Wireless Information and Power Transfer," *IEEE Workshop on Signal Processing Advances in Wireless Communications, SPAWC*, vol. 2019-July, 2019.

[19] D. H. Kim and J. I. Choi, "Design of a multiband frequency selective surface," *ETRI Journal*, vol. 28, no. 4, pp. 506–508, 2006.

[20] R. S. Anwar, L. Mao, and H. Ning, "Frequency selective surfaces: A review," *Applied Sciences (Switzerland)*, vol. 8, no. 9, pp. 1–47, 2018.

[21] T. J. Cui, M. Q. Qi, X. Wan, J. Zhao, and Q. Cheng, "Coding metamaterials, digital metamaterials and programmable metamaterials," *Light: Science & Applications*, vol. 3, no. 10, pp. e218–e218, 2014.

[22] C. Liaskos, S. Nie, A. Tsioliaridou, A. Pitsillides, S. Ioannidis, and I. Akyildiz, "Realizing Wireless Communication Through Software-Defined HyperSurface Environments," *19th IEEE International Symposium on a World of Wireless, Mobile and Multimedia Networks, WoWMoM 2018*, 2018.

[23] X. Tan, Z. Sun, D. Koutsonikolas, and J. M. Jornet, "Enabling Indoor Mobile Millimeter-wave Networks Based on Smart Reflect-arrays," *Proceedings - IEEE INFOCOM*, vol. 2018-April, pp. 270–278, 2018.

[24] Q. Wu and R. Zhang, "Intelligent Reflecting Surface Enhanced Wireless Network: Joint Active and Passive Beamforming Design," *IEEE Transactions on Wireless Communications*, vol. 18, no. 11, pp. 5394–5409, sep 2018. [Online]. Available: http://arxiv.org/abs/1809.01423

[25] ——, "Intelligent Reflecting Surface Enhanced Wireless Network via Joint Active and Passive Beamforming," *IEEE Transactions on Wireless Communications*, vol. 18, no. 11, pp. 5394–5409, 2019.

[26] ——, "Beamforming Optimization for Intelligent Reflecting Surface with Discrete Phase Shifts," in *ICASSP 2019 - 2019 IEEE International Conference on Acoustics, Speech and Signal Processing (ICASSP)*. IEEE, may 2019, pp. 7830–7833. [Online]. Available: https://ieeexplore.ieee.org/document/8683145/

[27] H. Guo, Y.-C. Liang, J. Chen, and E. G. Larsson, "Weighted Sum-Rate Optimization for Intelligent Reflecting Surface Enhanced Wireless Networks," pp. 1–13, 2019. [Online]. Available: http://arxiv.org/abs/1905.07920

[28] G. Zhou, C. Pan, H. Ren, K. Wang, and A. Nallanathan, "Intelligent Reflecting Surface Aided Multigroup Multicast MISO Communication Systems," *IEEE Transactions on Signal Processing*, vol. 68, pp. 3236–3251, 2020.

[29] M. Cui, G. Zhang, and R. Zhang, "Secure wireless communication via intelligent reflecting surface," *IEEE Wireless Communications Letters*, vol. 8, no. 5, pp. 1410–1414, 2019.

[30] Q.-U.-A. Nadeem, A. Kammoun, A. Chaaban, M. Debbah, and M.-S. Alouini, "Intelligent Reflecting Surface Assisted Wireless Communication: Modeling and Channel Estimation," pp. 1–7, 2019. [Online]. Available: http://arxiv.org/abs/1906.02360

[31] S. Abeywickrama, R. Zhang, and C. Yuen, "Intelligent Reflecting Surface: Practical Phase Shift Model and Beamforming Optimization," pp. 1–30, 2019. [Online]. Available: http://arxiv.org/abs/1907.06002

[32] Y. Yang, B. Zheng, S. Zhang, and R. Zhang, "Intelligent Reflecting Surface Meets OFDM: Protocol Design and Rate Maximization," pp. 1–32, 2019. [Online]. Available: http://arxiv.org/abs/1906.09956

[33] B. Zheng and R. Zhang, "Intelligent Reflecting Surface-Enhanced OFDM: Channel Estimation and Reflection Optimization," *IEEE Wireless Communications Letters*, pp. 1–1, 2019.

[34] Y. Yang, S. Zhang, and R. Zhang, "IRS-Enhanced OFDMA: Joint Resource Allocation and Passive Beamforming Optimization," *IEEE Wireless Communications Letters*, pp. 1–1, 2020.

[35] L. Dai, M. D. Renzo, C. B. Chae, L. Hanzo, B. Wang, M. Wang, X. Yang, J. Tan, S. Bi, S. Xu, F. Yang, and Z. Chen, "Reconfigurable Intelligent Surface-Based Wireless Communications: Antenna Design, Prototyping, and Experimental Results," *IEEE Access*, vol. 8, pp. 45 913–45 923, 2020.

[36] Q. Wu and R. Zhang, "Weighted Sum Power Maximization for Intelligent Reflecting Surface Aided SWIPT," *IEEE Wireless Communications Letters*, pp. 1–6, 2019.

[37] Y. Tang, G. Ma, H. Xie, J. Xu, and X. Han, "Joint Transmit and Reflective Beamforming Design for IRS-Assisted Multiuser MISO SWIPT Systems," 2019. [Online]. Available: http://arxiv.org/abs/1910.07156

[38] Q. Wu and R. Zhang, "Joint Active and Passive Beamforming Optimization for Intelligent Reflecting Surface Assisted SWIPT under QoS Constraints," pp. 1–30, 2019. [Online]. Available: http://arxiv.org/abs/1910.06220

[39] C. Pan, H. Ren, K. Wang, M. Elkashlan, A. Nallanathan, J. Wang, and L. Hanzo, "Intelligent Reflecting Surface Aided MIMO Broadcasting for Simultaneous Wireless Information and Power Transfer," pp. 1–33, 2019. [Online]. Available: http://arxiv.org/abs/1908.04863

[40] B. Clerckx, "Wireless Information and Power Transfer: Nonlinearity, Waveform Design, and Rate-Energy Tradeoff," *IEEE Transactions on Signal Processing*, vol. 66, no. 4, pp. 847–862, 2018.

[41] J. Hagerty, F. Helmbrecht, W. McCalpin, R. Zane, and Z. Popovic, "Recycling Ambient Microwave Energy With Broad-Band Rectenna Arrays," *IEEE Transactions on Microwave Theory and Techniques*, vol. 52, no. 3, pp. 1014–1024, mar 2004. [Online]. Available: http://ieeexplore.ieee.org/document/1273745/

[42] M. Piñuela, P. D. Mitcheson, and S. Lucyszyn, "Ambient RF energy harvesting in urban and semi-urban environments," *IEEE Transactions on Microwave Theory and Techniques*, vol. 61, no. 7, pp. 2715–2726, 2013.

[43] J. P. Curty, N. Joehl, F. Krummenacher, C. Dehollain, and M. J. Declercq, "A model for μ-power rectifier analysis and design," *IEEE Transactions on Circuits and Systems I: Regular Papers*, vol. 52, no. 12, pp. 2771–2779, 2005.

[44] Y. Huang and B. Clerckx, "Large-Scale Multiantenna Multisine Wireless Power Transfer," *IEEE Transactions on Signal Processing*, vol. 65, no. 21, pp. 5812–5827, 2017.

[45] T. Adali and S. Haykin, *Adaptive Signal Processing*. Hoboken, NJ, USA: John Wiley & Sons, Inc., mar 2010. [Online]. Available: http://doi.wiley.com/10.1002/9780470575758

[46] M. C. Grant and S. P. Boyd, "The CVX Users ' Guide, Release 2.0 (beta)," vol. 0, 2013.

[47] Y. Huang and D. P. Palomar, "Rank-constrained separable semidefinite programming with applications to optimal beamforming," *IEEE Transactions on Signal Processing*, vol. 58, no. 2, pp. 664–678, 2010.

[48] S. Boyd, S. J. Kim, L. Vandenberghe, and A. Hassibi, "A tutorial on geometric programming," *Optimization and Engineering*, vol. 8, no. 1, pp. 67–127, 2007.

[49] M. Chiang, *Geometric programming for communication systems*, 2005, vol. 2, no. 1.

[50] B. R. Marks and G. P. Wright, "A General Inner Approximation Algorithm for Nonconvex Mathematical Programs," *Operations Research*, vol. 26, no. 4, pp. 681–683, 1978.

[51] W. C. Li, T. H. Chang, C. Lin, and C. Y. Chi, "Coordinated beamforming for multiuser MISO interference channel under rate outage constraints," *IEEE Transactions on Signal Processing*, vol. 61, no. 5, pp. 1087–1103, 2013.

[52] L. Grippo and M. Sciandrone, "On the convergence of the block nonlinear Gauss-Seidel method under convex constraints," *Operations Research Letters*, vol. 26, no. 3, pp. 127–136, 2000.

[53] M. Hong, M. Razaviyayn, Z. Q. Luo, and J. S. Pang, "A Unified Algorithmic Framework for Block-Structured Optimization Involving Big Data: With applications in machine learning and signal processing," *IEEE Signal Processing Magazine*, vol. 33, no. 1, pp. 57–77, 2016.

[54] Q. Li, M. Hong, H. T. Wai, Y. F. Liu, W. K. Ma, and Z. Q. Luo, "Transmit solutions for MIMO wiretap channels using alternating optimization," *IEEE Journal on Selected Areas in Communications*, vol. 31, no. 9, pp. 1714–1727, 2013.

[55] V. Erceg, L. Schumacher, P. Kyritsi, A. F. Molisch, D. S. Baum, A. Y. Gorokhov, C. Oestges, Q. Li, K. Yu, N. Tal, and B. Dijkstra, "IEEE P802.11 TGn Channel Models," *IEEE 802.11-03/940r4*, no. May, pp. 1–45, 2004.